Physical Models for Simulation and Reconstruction of Human Tissue Deformation Fields in Dynamic MRI

Erlend Hodneland*, Erik Hanson, Antonella Z. Munthe-Kaas, Arvid Lundervold, *Member, IEEE*, and Jan M. Nordbotten

***Abstract*— *Objective:* Medical image registration can be formulated as a tissue deformation problem, where parameter estimation methods are used to obtain the inverse deformation. However, there is limited knowledge about the ability to recover an unknown deformation. The main objective of this study is to estimate the quality of a restored deformation field obtained from image registration of dynamic MR sequences. *Methods:* We investigate the behavior of forward deformation models of various complexities. Further, we study the accuracy of restored inverse deformations generated by image registration. *Results:* We found that the choice of 1) heterogeneous tissue parameters and 2) a poroelastic (instead of elastic) model had significant impact on the forward deformation. In the image registration problem, both 1) and 2) were found not to be significant. Here, the presence of image features were dominating the performance. We also found that existing algorithms will align images with high precision while at the same time obtain a deformation field with a relative error of 40%. *Conclusion:* Image registration can only moderately well restore the true deformation field. Still, estimation of volume changes instead of deformation fields can be fairly accurate and may represent a proxy for variations in tissue characteristics. Volume changes remain essentially unchanged under choice of discretization and the prevalence of pronounced image features. *Significance:* We suggest that image registration of high-contrast MR images has potential to be used as a tool to produce imaging biomarkers sensitive to pathology affecting tissue stiffness.**

***Index Terms*—Biot equations, dynamic imaging, elasticity, heterogeneity, image registration.**

I. Introduction

MEDICAL image registration is the task of aligning images, either within a time series or between multimodal image acquisitions [1]. In this study, we focus on the alignment of time series through estimation of tissue or organ deformation fields. For such problems, the objects of interest are captured within a sequence of images over time, where each frame needs to be aligned with a common reference (target) image for further analysis. After application of the obtained deformation field, the corresponding objects in all input images should be spatially aligned with the corresponding objects in the reference image. After this alignment, a successful image registration enables a thorough voxel-by-voxel comparison of object properties throughout the time series [2].

The image registration problem is by nature an ill-posed inverse problem. In general, there is no unique deformation field representing the correct alignment of images. Therefore, a method for image registration has normally two components, a data term and a regularization term. The data term measures similarity between the input and the target image, and the regularization term reduces the ill-posedness of the inverse problem [3]. The regularization can also be thought of as the deformation model as it represents a set of rules or constraints for the deformation. In this study, we extend the concept of image registration to not only be a method for image alignment, but also to become the task of model-based estimation of a physical deformation that has occurred during the observation period (image time series). Human organs and tissue obey the laws of physics in their process of their deformation. As a consequence, it is natural to use image registration regularizers originating from physical deformation models. As a direct consequence of this, we explore linear elasticity known from continuum mechanics as a model for deformation of elastic objects. Every living body part or organ can be assigned a set of tissue parameters reflecting its elastic properties. The Lamé parameters and the porosity are examples of such parameters. The Lamé parameters are essential components of linear elasticity, and are in many image registration contexts referred to as "regularization parameters" rather than "tissue parameters." The term "regularization parameters" is clearly more appropriate in combination with nonphysical deformation models. However, within our context of establishing a highly physical image registration model, we consider the term "tissue parameters" to be more descriptive.

A wide range of mechanical models have been investigated for human tissue, including nonlinear and viscoelastic models [4], [5]. Mechanical complexity for human cartilage was demonstrated in [6], showing anisotropy, inhomogeneity, and tension-compression nonlinearities. Linear elasticity was recognized as a reasonable approximation to soft tissue deformation in [7], and further extended to nonlinear viscoelasticity in [8]. These references highlight the complex

Manuscript received July 7, 2015; accepted December 30, 2015. Date of publication January 4, 2016; date of current version September 16, 2016. *Asterisk indicates corresponding author*

*E. Hodneland is with the Christian Michelsen Research and MedViz Research Cluster, 5072 Bergen, Norway, and also with University of Bergen, 5020 Bergen, Norway (e-mail: erlend.hodneland@gmail.com).

E. A. Hanson and A. Z. Munthe-Kaas are with the Department of Mathematics, University of Bergen.

A. Lundervold is with the Department of Biomedicine, University of Bergen and the Department of Radiology, Haukeland University Hospital.

J. M. Nordbotten is with the Department of Mathematics, University of Bergen, Norway, and with Department of Civil and Environmental Engineering, Princeton University.

Color versions of one or more of the figures in this paper are available online at http://ieeexplore.ieee.org.

Digital Object Identifier 10.1109/TBME.2015.2514262

challenges encountered in mechanical modeling of the highly heterogeneous human abdomen. Without access to accurate segmentations, a locally optimal deformation model is ambitious to implement for all tissue simultaneously. Additionally, there are numerical challenges related to stability and convergence when combining models across tissue. Thus, as a first step deformation model for the human abdomen, we apply linear (poro-) elasticity to the entire domain, which is considered a reasonable approximation to a wide range of deformation events [9], including small deformations in human soft tissue [8].

In order to be able to use image registration as a biomarker for altered tissue stiffness, a reconstructed deformation field of high quality is probably crucial. Estimating the reconstruction error is, therefore, a major issue and a motivation for this study. Our aim is to identify factors that are important for reconstructing an authentic or plausible deformation field. In this process, we have considered on a set of factors related to heterogeneity in the tissue stiffness and in fluid permeability parameters, various physically deformation models, effects from undersampling in k-space, as well as a gridding pattern of the image. In the following, we describe these factors in more detail.

The human abdominal region, ranging from soft tissue (viscera) to bone (columna), is highly varying in terms of stiffness. Thus, it is reasonable to use heterogeneous tissue parameters in an image registration method. Such methods typically employ the same parameters for the whole image [10] and heterogeneity versus homogeneity in the image registration has not been thoroughly investigated. Related to heterogeneous tissue parameters is the usage of locally adaptive regularization parameters [11], [12]. Also anisotropic models have been proposed [11], [13]. However, these approaches are either coupled to image intensities and are therefore not directly reflecting stiffness of the underlying tissue, or they are aiming at preserving prescribed properties of the deformation field, like anisotropy.

As a further extension to tissue heterogeneity in the model, one can consider parameters varying also locally within the same tissue, as a result of the complex biomechanical architecture of organs. We refer to this situation as "irregularities" within the tissue parameters.

Human tissue is simultaneously deformable and highly porous. The porous properties are due to the fluid-filled network of capillaries and lumina. From a physical perspective, these properties advocate a deformation model accounting for the interaction between mechanical forces and fluid flow. Such a model, known as poroelasticity or the Biot equations [14], is our default deformation model in this study, where the use of poroelasticity as a deformation model for image registration is a novel contribution. On the other hand, outside the image processing applications, poroelasticity is an increasingly popular deformation model of human tissue. A spatiotemporal, poroelastic, hemodynamic model was used to create a theoretical foundation for understanding the hemodynamic responses [15]. A model for poroelasticity was also proposed for simulations on how changes in fluid reabsorption can be responsible for enlargement of the ventricles in hydrocephalic brain dynamics, both in human [16] and in cat [17]. In [18], poroelasticity was applied to model the ischemia-reperfusion injury by tissue swelling and a secondary vessel collapse. Significant changes of strain in the human brain upon forced expiration were shown in [19], and the authors concluded that the relatively frequent findings of volumetric strain are due to the poroelastic nature of the human brain. As a model for soft arteries, Simon et al. [20] considered a soft hydrated tissue material composed of an incompressible porous solid (fibrous matrix) saturated by an incompressible fluid (water). In [21], the porous spinal cord was modeled as a poroelastic medium. Also in geomechanics, many poroelastic models have been described [22], [23].

Volume changes are expected to vary significantly between linear elasticity and poroelasticity. Volume changes in a perfused object either occur from compression/decompression, and/or by inflow or outflow of fluid or gas from a cavity, or physiologically controlled volume. Assuming no pockets of gas, thereby excluding the lungs from our model, the compression of fluid or solid is almost negligible in human tissue due to incompressibility of water. Thereby, volume changes associated with inflow or outflow of fluid from a control volume can possibly occur in highly perfused human tissue by two means, as described in Fig. 1. First, an external pressure arising from breathing, striate muscle contractions, movement in the gravitational field, the cardiac cycle, or intestinal peristalsis, can locally change the rate of blood flow within the capillary bed in an organ. A secondary effect of this motion is local volume changes arising from redistribution of fluid within the organ. Second, there is a possibility of a global volume change of the organ, arising from an external pressure gradient leading to a change in the steady-state inflow and outflow of blood and other fluid components. The viscous fluid will in this sense act as a damping force on the deforming object. Owing to the ability of poroelasticity to accurately model the capacity of human tissue to undergo such volume changes, we suggest to use this as a metric to identify pathological variations of viscous effects.

The prescribed factors of heterogeneous tissue parameters and the use of poroelasticity as a deformation model are directly coupled to the discretization and numerics, and will, therefore, affect both a forward simulation as well as a reconstruction by image registration. The next two factors we describe are not related to physical assumptions about the tissue, but rather reflected in the registration force for reconstruction. Undersampling in k-space[1] is one such factor, widely used in fast dynamic MR sequences for perfusion measurements. The amount of undersampling in k-space is a matter of time efficiency and robustness toward motion artifacts. It is not known to what extent this type of artifacts will influence the registration performance, and in this study, we investigate the effect of such undersampling.

Another option to possibly improve the registration quality is to use MR sequences maximizing the image contrast, leading to a stronger registration force as the data term is depending on contrast and image features. Artificially imposing contrast is thus possible via an MR sequence allowing for magnetic tagging [24]–[26]. In this technique, magnetic tags are imposed within the tissue from locally induced perturbations of the magnetization. These locations of altered magnetization are visible in the MR image for a limited amount of time, and are therefore, useful to determine the deformation. In order to mimic

[1]That is, undersampling the Fourier expansion coefficients of the signal

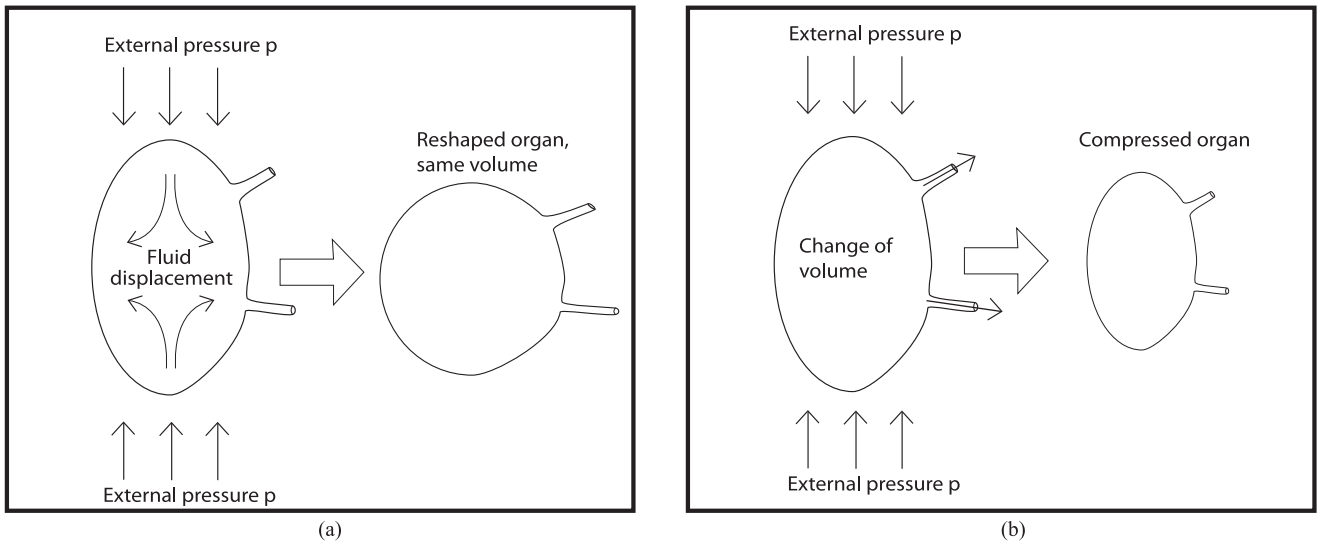

Fig. 1. Displacement modes of a poroelastic organ exposed to external, uniaxial pressure. The deformable organ displacement can be split into two components: isovolumetric deformation with internal fluid displacement (A) and isomorphic compression with volume changes (B). Both displacement modes include a net fluid transport, either dislocation of fluid within the organ (deformations) or a net in/out flux of fluid from the organ. Applied to the kidneys and other parenchymal organs like the liver, the spleen, the gastrointestinal tract, the pancreas, and the heart, contraction and compression of perfused and deformable tissue can be modeled by poroelasticity.

a situation of maximal image contrast, and thus, ascertain the potential benefit of this approach, we imposed a regular grid of low intensities, and investigated whether such gridding has a potential to improve the recovered deformation field.

The main contribution of this study is to evaluate the accuracy of the restored deformation field from registration. By the combination of all investigated factors, as well as chosen values of temporal and spatial resolution, we have created a digital phantom meant to cover the characteristics encountered in a typical, dynamic MR scan, and thereby, generate results that can be transferrable to real MR scans of patients. From an automatic or manual organ segmentation and the estimated deformation field by registration, it is thereby possible to extract organ characteristics with the aim of identifying pathological tissue like fibrosis, where changes in tissue stiffness occur. By these means, standard T1-weighted, dynamic MRI protocols for *in vivo* measurements of tissue stiffness, without injecting a contrast agent as in DCE- or DSC-MRI, could have the potential to become a complementary tool to MR elastography (MRE) as a biomarker for characterization of pathological tissue [27].

The rest of this paper is organized as follows. In Section II-A, we describe the poroelastic model in terms of the momentum equations, Darcy's law, and the continuity equation. A digital phantom is introduced in Section III, and a forward simulation is performed in Section III-B based on this phantom. image registration is conducted in order to restore the inverse deformation field. A comparison of the deformation fields upon various model conditions and configurations is reported in Section IV, and finally, conclusions are given in Sections V–VI.

II. Mathematical Approach

A. Poroelastic Model for Deformations

To improve and extend linear elasticity into a physically even more plausible model for deformation of human tissue, we take jointly into account elastic and porous properties of the tissue. The poroelastic model is derived using three well-known physical principles, conservation of momentum, mass balance, and Darcy's law. We define the porosity

$$\phi = \frac{V_f}{V} \tag{1}$$

as a measure of relative fluid volume V_f inside a control volume V. The fluid volume V_f here denotes the fluid fraction that is permitted to move, in particular, the vascular fluid being transported in the porous capillary system. Thus, fluid with highly restricted motion, i.e., residing inside cells, is not accounted for in the porosity. We assume full saturation of the pore space, implying no vacuum or air pockets.

We let $\vec{u} : \Omega \times T \to \mathbb{R}^3$ denote a deformation vector field, being a function of a spatial domain $\Omega \subset \mathbb{R}^3$ with boundary Γ and a time span $T \subseteq \mathbb{R}^+$. In linear elasticity, the Lagrangian strain tensor is approximated by the linearized strain tensor

$$\boldsymbol{\epsilon} = \frac{1}{2}\left(\nabla\vec{u} + (\nabla\vec{u})^T\right) \tag{2}$$

valid for small deformation gradients [9]. The stress tensor $\boldsymbol{\sigma} = \boldsymbol{C} : \boldsymbol{\epsilon}$ is a generalization of Hooks law for the material stiffness tensor $\boldsymbol{C}$. Thus, $\boldsymbol{\sigma} = 2\mu\boldsymbol{\epsilon} + \lambda(tr\boldsymbol{\epsilon})\boldsymbol{I}$ [9], where $\lambda : \Omega \to \mathbb{R}$ is the first Lamé constant, $\mu : \Omega \to \mathbb{R}$ is the second Lamé constant or shear modulus. In the poroelastic description, one allows for an extra diagonal term, coming from the hydrostatic pressure $p : \Omega \times T \to \mathbb{R}$ of fluid in the pores [23]. This results in the poroelastic constitutive equations

$$\boldsymbol{\sigma} = 2\mu\boldsymbol{\epsilon} + \lambda(tr\ \boldsymbol{\epsilon})\,\mathbf{I} - \alpha p\boldsymbol{I} \tag{3}$$

for the identity $\boldsymbol{I}$. Given an external force field $\vec{b}(\vec{x}, \vec{u})$ representing volume forces with a global scaling factor γ, the conservation of momentum states that for an object with zero acceleration the sum of forces per unit volume is equal to zero [9], thus

$$\nabla \cdot \boldsymbol{\sigma} + \gamma\vec{b}(\vec{x}, \vec{u}) = 0. \tag{4}$$

Mass balance of the fluid flow is ensured by the continuity equation, expressed in global form as

$$\frac{d}{dt}\int_{\Omega_i}\phi\rho d\vec{x}+\int_{\Gamma_i}\rho\vec{q}\cdot\vec{e}_n dS=0 \tag{5}$$

for a geometric control volume Ω_i with boundaries Γ_i. Here, $\vec{e}_n$ is the outer unit normal vector of Γ_i, $\vec{q}:\Omega\times T\rightarrow\mathbb{R}^3$ is the flux per unit area $[\mathrm{m}^3/\mathrm{s}/\mathrm{m}^2]$, and $\rho:\Omega\times T\rightarrow\mathbb{R}$ is the fluid density $[\mathrm{kg}/\mathrm{m}^3]$. Equation (5) must be valid for every geometric control volume Ω_i, hence, by the divergence theorem, one obtains the local form

$$\frac{\partial}{\partial t}(\phi\rho)+\nabla\cdot(\rho\vec{q})=0. \tag{6}$$

Assuming a weakly linear and isothermal relationship between the density ρ and pressure p, we can phrase density as a function of pressure as $\rho(\vec{x},t)=\beta p(\vec{x},t)+c_1$ for a small constant β and a constant c_1. Furthermore, one can assume that porosity of the tissue is essentially a linear function of the volume change $\nabla\cdot\vec{u}$, which is the process leading to local inflow or outflow of fluid. Thus, one can expect a relationship $\phi=\alpha\nabla\cdot\vec{u}+c_2$ for a scaling factor α and a constant c_2. The constant α is the fraction of volume change that leads to change in porosity, and can be set to $\alpha\approx 1$ for human parenchymal tissue where basically the complete volume change will lead to a corresponding change in porosity and inflow of fluid. An exception to this assumption occurs in the lungs where the volume change leads to inflow of compressible fluid (air). Embedding these assumptions and using the chain rule to the first term in (6) we obtain

$$\frac{\partial}{\partial t}(\phi\rho)=\phi\beta\frac{\partial p}{\partial t}+\rho\alpha\frac{\partial}{\partial t}(\nabla\cdot\vec{u}). \tag{7}$$

Using a Boussinesq approximation, we will assume that the spatial variation of the density ρ is sufficiently small to be neglected $\nabla\rho=0$, thus the continuity equation (6) can be expressed as

$$\chi\frac{\partial p}{\partial t}+\rho\alpha\frac{\partial}{\partial t}(\nabla\cdot\vec{u})+\rho\nabla\cdot\vec{q}=0 \tag{8}$$

for a small and arbitrary $\chi\equiv\phi\beta$, where β is a small, unknown constant.

Further, porous media fluid flow is macroscopically described by Darcy's law. Assuming laminar flow, the flux $\vec{q}$ is proportional to the pressure gradient, the gravitational field, the permeability k $[m^2]$, and inverse proportional to the fluid viscosity μ_b $[Pa\cdot s]$

$$\vec{q}=-\frac{k}{\mu_b}(\nabla p-\rho g\vec{e}_z) \tag{9}$$

where g is the gravitational acceleration along the unit vector $\vec{e}_z$. The gravitational term will be neglected under the assumption that the gravitational acceleration is approximately constant across the characteristic length scale of the organ of interest, Provided a nonzero density ρ and combining Darcy's law (9) with the continuity equation (8) we obtain the flow equation

$$-\nabla\cdot\left(\frac{k}{\mu_b}\nabla p\right)+\frac{\chi}{\rho}\frac{\partial p}{\partial t}+\alpha\frac{\partial}{\partial t}(\nabla\cdot\vec{u})=0. \tag{10}$$

Note that in (10), the pressure can only be estimated up to a constant p_0, and any solution can be replaced by $p\rightarrow p+p_0$, depending on the Dirichlet boundary conditions. However, the Dirichlet boundary conditions are essentially unknown and we can, therefore, only estimate a bias pressure field deviating from the steady-state pressure. Combining (10) with the three equations for conservation of momentum (4), we now have a complete set of four equations for the unknowns $\vec{u}$ and p of the poroelastic model. Settings $\alpha=0$ and discarding the flow equation (10) leads to the equations of linear elasticity.

TABLE I
TISSUE PARAMETERS USED FOR GENERATING THE DIGITAL PHANTOM

Parameter	Unit	Kidney	"Generic Organ"	Spine
λ	kPa	0.01	0.01	5.55×10^4 [34]
μ	kPa	1.67 [27]	0.41 [35]	8.33×10^4 [34]
k	m^2	0.26×10^{-12}	0.13×10^{-12}	0.26×10^{-15}

The "generic organ" is a combination of soft tissue like liver and the spleen, typically less perfused than the kidneys. For the homogeneous model, the Lamé constants of the kidneys were used everywhere, while for the heterogeneous model, local parameters were assigned according to the segmentation mask. λ = First Lamé parameter, μ = shear modulus, k = permeability.

III. Digital Phantom and Numerical Implementation

An *in silico* kidney phantom in 2-D was created using several different modeling and imaging assumptions. The dynamics of the phantom was generated by a dynamic force resulting in time-dependent deformation fields and a deforming image time series. The deformed time series was used as input for the reconstruction of the (inverse) deformation field by image registration. The relative error of the reconstruction is reported and was used to classify various experimental setups within image registration models in terms of their impact on registration accuracy.

A. Digital Phantom

The noise-free digital phantom consists of a synthetic MR image $f(\vec{x},t)$ (2-D + time) containing realistic MR signal intensities, as well as 2-D tissue parameter maps of $\mu(\vec{x}),\lambda(\vec{x})$ and $k(\vec{x})$. The phantom was constructed in the following way. An existing 3-D+time DCE-MRI dataset of a healthy volunteer was manually segmented into four regions: spine, whole kidney, kidney cortex, and "generic organ." The segmentation was used to create a time series of spatially realistic MR intensities $f(\vec{x},t)$. To construct $f(\vec{x},t)$, we selected a frame in the original DCE-MRI time series and computed the average intensity within each region of the segmentation. This regional intensity value was assigned to $f(\vec{x},T_0)$ and duplicated along the time axis with a temporal resolution of $\Delta t=0.25\,s$ to create a "monomodal" time series suitable for registration with a sum-of-squared differences (SSD) cost function. The time series $f(\vec{x},t)$ was used as input to the forward deformation and subsequent reconstruction by registration. The segmentation was also used to spatially assign space-dependent Lamé constants within the parameter maps of $\mu(\vec{x}),\lambda(\vec{x})$, and $k(\vec{x})$ (cfr., Table I). The liver was used as a model organ to assign Lamé constants and permeability k within the "generic organ" class. The time series $f(\vec{x},t)$, and

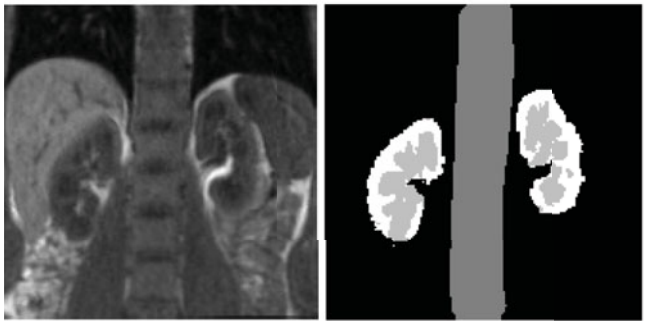

Fig. 2. Left: DCE-MRI image used for creating the geometry of the digital phantom. Right: Segmentation of the MR image. Tissue specific regional intensities and Lamé parameters were assigned according to the segmentation.

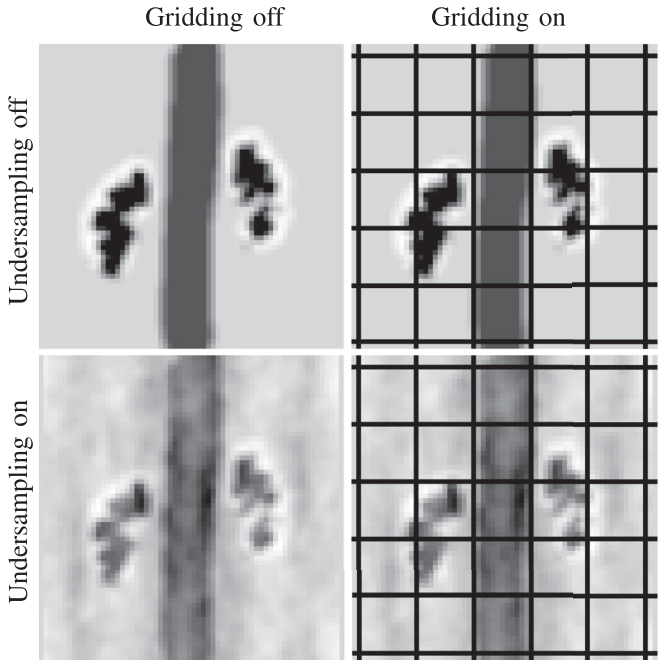

Fig. 3. Images used for forward deformation. Left to right: Image $f(\vec{x}, T_0)$ without (left) and with (right) gridding pattern. Top to bottom: Fully sampled and undersampled k-space. For the lower right image, the gridding pattern was imposed after undersampling, hence, the grid lines themselves are free of noise.

the parameter maps $\mu(\vec{x}), \lambda(\vec{x})$, and $k(\vec{x})$ were convolved with a Gaussian kernel of diameter $11\,\mathrm{mm}$ and standard deviation of $8\,\mathrm{mm}$ in order to simulate partial volume effects. Further, all images were cropped to a field of view (FOV) consistent with the domain $\Omega = \{x_1, x_2 : 0 \leq x_1 \leq 0.27\,\mathrm{m}, 0 \leq x_2 \leq 0.27\,\mathrm{m}\}$, and resampled to a 2-D grid with resolution $N = (64, 64)$ of equally shaped, rectangular pixels. The real MR image as well as the segmentation, used to create the digital phantom, are shown in Fig. 2. The obtained noise free synthetic MR image of intensities is shown in the upper left panel of Fig. 3, showing the two kidneys and the spine.

1) Toggling Features of the Digital Phantom: A set of image features, controlled by a ON/OFF switch, was added to the phantom to simulate undersampling in k-space and a situation of maximal contrast features.

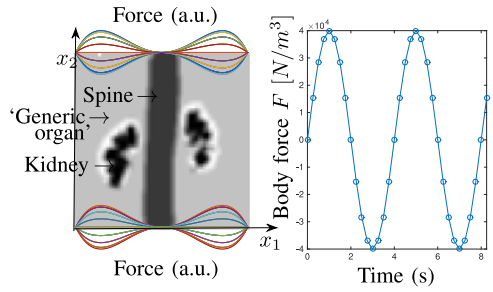

Fig. 4. Deforming the digital MR image used for evaluation of image registration. Left: Average image intensities within a segmentation map were computed from a selected time point in a real DCE-MRI time series, and the average intensity values within each segmented region were assigned to their respective regions. The image was duplicated along the time axis to create a time series for registration, which was exposed to a time varying force simulating periodic forces arising due to breathing. The spatial distribution of the force is plotted with various colors, corresponding to different time points. Right: The periodic body force as a function of time for the selected pixel in the phantom highlighted with white (left panel). Circle markers indicate discrete time points used in the simulations ($\Delta t = 0.25$ s).

1) *Undersampling in k-space*: We constructed one phantom without undersampling in k-space ("Undersampling OFF"), resulting in signal-to-noise ratio $\mathrm{SNR} \to Inf$, and one phantom with undersampling ("Undersampling ON"), with a $\mathrm{SNR} = 32$. Signal to noise ratio was computed as $\mathrm{SNR} = \tilde{\mu}/\sigma$ for the average image value $\tilde{\mu}$ and standard deviation σ of the noise. For "Undersampling ON," the Fourier transform of $f(\vec{x}, t)$ was computed and 30% of the pixels in Fourier space (or k-space) were replaced by zeros. The image was then reconstructed by the inverse Fourier transform. Every time point in the time series had a different noise pattern since different frequencies were replaced by zero.
2) *Gridding Pattern*: We constructed a phantom without ("Grid OFF") and with a gridding pattern ("Grid ON"). The gridding pattern was created in order to simulate optimal registration performance with maximally structural information present. Additionally, the gridding pattern has a visual similarity to patterns created by real MR tagging sequences [24]–[26]. To create the gridding pattern, a rectangular square pattern with a spacing of $0.05\,\mathrm{m}$ and intensity value $0.95 \min_{\vec{x}} f(\vec{x}, T_0)$ was imposed on $f(\vec{x}, t)$.

Toggling ON and OFF the undersampling and tagging features resulted in four different image types, as shown in Fig. 3. We defined "Undersampling ON" and "Gridding OFF" to be the default configuration for a standard dynamic MR acquisition.

B. Deformation of the MR Phantom

A deformed phantom $f(\vec{x} + \vec{u}(\vec{x}, t), t)$ was generated using a body force $\vec{F}(\vec{x}, t) = (F_1(\vec{x}, t), F_2(\vec{x}, t))^T$ mimicking breathing. In a Cartesian coordinate system (see Fig. 4, left panel), $\vec{F}(\vec{x}, t)$ was defined to be zero in the horizontal component ($F_1(\vec{x}, t) = 0$), and to be a fourth-order polynomial in the x_1-variable in the vertical component $F_2(\vec{x}, t)$. A further sine modulation was added to simulate the periodicity of respiration.

Explicitly

$$F_2(\vec{x},t) = -\frac{4M}{(D/2)^4}\sin(wt)\left(x_1^2-(D/2)^2\right)x_1^2, \quad \vec{x}\in[0,D]^2 \tag{11}$$

with $M = 40\,\mathrm{kN/m^3}$, frequency $w = \pi/2\,\mathrm{Hz}$, and $D = 0.27\,\mathrm{m}$ denoting the physical width of the domain. Note that this choice gives $F_2(\vec{x},t) = 0$ for $\vec{x} = (0, x_2)$ (left boundary), $\vec{x} = (D/2, x_2)$ (spine vertical axis), and $\vec{x} = (D, x_2)$ (right boundary). The maxima are located between the spine vertical axis and left and right boundary, respectively, and satisfy the condition $\max_{x_1} F_2(\vec{x},t) = M\sin(wt)$.

C. Numerical Modeling

The poroelastic equations were numerically solved using multipoint stress approximation (MPSA) [28], [29]. MPSA is an extension of multipoint flux approximation (MPFA) scheme developed for flow simulations in porous media [30]. It allows for tensor-valued strain $\boldsymbol{\epsilon}$ instead of vector-valued flux. The stability and accuracy of MPSA was previously shown for elasticity [28] as well as for combined poroelastic (hydromechanical) simulations [29]. Particularly favorable about the MPSA framework is its ability to handle challenging numerical conditions following strong discontinuities in the Lamé constants and permeability, without entering numerical instability. This property is essential in our numerical simulations where we assign realistic and therefore strongly varying tissue parameters to solid bone compared to soft tissue. The MPSA framework was applied in the forward simulations, as well as for registration, referred to as "Biot registration."

Denote by $\vec{\mathcal{U}}^n$ and $\vec{\mathcal{P}}^n$ the concatenation of the deformation field $\vec{u}$ and pressure p at iteration n into a long vector, respectively. Similarly, let $\vec{\mathcal{F}}$ be a concatenation of the body force field across the entire image domain. Discretization of the poroelastic equations (3), (4), and (10) using MPSA resulted in a linear system

$$\begin{pmatrix} \mathbf{E} & -\alpha\mathbf{D} \\ -\alpha\mathbf{D}^T & \mathbf{K} \end{pmatrix}\begin{pmatrix} \vec{\mathcal{U}}^{(n)} \\ \vec{\mathcal{P}}^{(n)} \end{pmatrix} = \begin{pmatrix} 0 & 0 \\ -\alpha\mathbf{D}^T & \frac{\chi}{\rho}\boldsymbol{I} \end{pmatrix}\begin{pmatrix} \vec{\mathcal{U}}^{(n-1)} \\ \vec{\mathcal{P}}^{(n-1)} \end{pmatrix} - \begin{pmatrix} \vec{\mathcal{F}}^{(n-1)} \\ 0 \end{pmatrix} \tag{12}$$

which was solved for each time point, and where $\mathbf{K} = \frac{k\Delta t}{\mu_b}\mathbf{D}^T\mathbf{D} + \frac{\chi}{\rho}\boldsymbol{I}$ for the gradient operator $\mathbf{D}$. Renaming the left-hand side and right-hand side matrices as $\mathcal{A}_1, \mathcal{A}_2$, the linear system can be written more compactly as

$$\mathcal{A}_1\begin{pmatrix} \vec{\mathcal{U}}^{(n)} \\ \vec{\mathcal{P}}^{(n)} \end{pmatrix} = \mathcal{A}_2\begin{pmatrix} \vec{\mathcal{U}}^{(n-1)} \\ \vec{\mathcal{P}}^{(n-1)} \end{pmatrix} - \begin{pmatrix} \vec{\mathcal{F}}^{(n-1)} \\ 0 \end{pmatrix}. \tag{13}$$

1) Tissue Parameters: We applied a simplified model to estimate the permeability of porous parenchymal organs due to lack of reasonable literature values. For this estimation, we used Darcy's law in a scalar setting, stating that total flow Q $[m^3/s]$ divided by the area A is related to blood viscosity μ, permeability k, pressure drop Δp, and length ΔL by the relation

$$\frac{Q}{A} = -\frac{k}{\mu}\frac{\Delta p}{\Delta L}. \tag{14}$$

Using the kidney as a model system, the flux is approximately $0.625\,\mathrm{L/min}$ for a kidney with a cross-sectional area similar to an ellipsoid with half axes 5.5 and $3\,\mathrm{cm}$ [31]. The estimated value for blood viscosity is given in Table I, which is taken as a dynamic viscosity changing with shear rate since blood is a non-Newtonian fluid. The largest pressure drop in the kidney of $\Delta p = 6.66\,\mathrm{kPa}$ [32] takes place along the afferent arterioles with length of approximately $0.17\,\mathrm{mm}$ [33]. Applying (14), we obtain an estimate for the permeability of $k_{\mathrm{kidney}} = 0.26\times10^{-12}\,\mathrm{m}^2$. For the spine we used a value of order $k_{\mathrm{kidney}}\times\ 10^{-3}$, and "generic organ" was assigned a permeability of $k_{\mathrm{kidney}}/2$ due to the lower perfusion of surrounding tissue in comparison to the kidneys. Values of λ and μ reported in [34] were for cortical bone, and our parameters for the spine were, therefore, rescaled with a factor 10^{-2} to account for the softer matrix properties of intervertebral disks than bone only. We used low values of $\lambda_{\mathrm{kidney}}$ due to the porous properties of the kidneys, only weakly resisting a compression if the fluid is removed. The values of the shear modulus were unchanged compared to literature reference values.

2) Boundary Conditions: Dirichlet boundary conditions $\vec{u} = 0$ of the forward simulation as well as the backward reconstruction were used for the domain $\{\vec{x} : x_2 = 0\}$. Elsewhere, Neumann boundary conditions $\nabla\vec{u}\cdot\vec{n} = 0$ where imposed. Here, $\vec{n}$ is the outward normal vector of Ω. For the pressure p, Neumann boundary conditions $\nabla p\cdot\vec{n} = 0$ were imposed everywhere. These boundary conditions are simulating a freely moving surface everywhere except within the immobilized matrix associated with the lower abdomen.

3) Varying the Model Complexity: We explored the effect of a set of parameter choices on both the forward simulation and backward reconstruction.

1) *Spatial heteregeneous Lamé constants and permeability* k: We explored the deformation models (2)–(4) and (10) for regional valued $\mu = \mu(\vec{x}), \lambda = \lambda(\vec{x}), k = k(\vec{x})$ ("Heterogeneous ON"), or spatially constant tissue parameters ("Heterogeneous OFF").
2) *Poroelasticity*: We investigated various deformation models according to poroelasticity ("Poroelasticity ON," $\alpha = 1$), or linear elasticity ("Poroelasticity OFF," $\alpha = 0$).
3) *Irregularities in the tissue parameters*: Irregular ("Irreg = ON") and regular ("Irreg OFF") Lamé parameters and permeability k within each tissue type. To create irregular parameter maps, each of the maps $\mu(\vec{x}), \lambda(\vec{x})$, and $k(\vec{x})$ were multiplied by a standard uniform distribution of average 1 on the interval $[0.5, 1.5]$, followed by a Gaussian filter with radius $12\,\mathrm{mm}$ and standard deviation $4\,\mathrm{mm}$.

Thus, a total of eight combinations of the three binary conditions ("heterogeneity," "poroelasticity," and "irregularity") resulted in eight distinct discretization matrices, and thereby, eight distinct forward transformations. We defined a *default discretization* to be the physically most realistic configuration: "Heterogeneous ON," "Poroelasticity ON" and "Irreg ON."

Variations on these switches were compared to the default configuration.

D. Reconstruction by Image Registration

From each of the eight combinations above and the four time series with and without noise and gridding, we generated a total of 32 different cases for reconstruction. The reconstruction by image registration was performed on the forward simulated image created with the default discretization, and the body force for reconstruction was the functional derivative of the SSD cost function (15),

$$F_{\mathrm{SSD}}(\vec{u}) = \frac{1}{2}\int_{\Omega}(f(\vec{x}+\vec{u},t) - f_r(\vec{x}))^2 d\vec{x} \tag{15}$$

becoming $\vec{\mathcal{F}}^{(n-1)}$ in (13). We used a scaling factor for SSD of $\gamma = 5 \times 10^3$. The resulting nonlinear system of equations was solved by fixed point iterations An additional Tikhonov regularization for numerical stabilization was also applied, such that $\mathcal{A}_i \leftarrow \mathcal{A}_i - \beta \boldsymbol{I}$ for a suitable $\beta \in \mathbb{R}^+$.

E. Metrics for Evaluation Comparison of Deformation Fields

Unlike classical evaluation of image registration, where only the final alignment of images is measured, we will now require evaluation tools suitable for comparing deformation fields. The tools will be used both to compare forward deformation models and the different image registration methods.

1) Comparing the Forward Deformation Fields to the Deformation Field of the Default Configuration: Denote by $\vec{u}_d$ the deformation field of the *default* configuration. We measure the absolute, relative differences in the deformation fields within different discretization scenarios as

$$E_{\mathrm{forw}}(\vec{u},\vec{u}_d) = \sqrt{\frac{\sum_{\vec{X}_i\in\Omega}|\vec{u}(\vec{X}_i) - \vec{u}_d(\vec{X}_i)|^2}{\sum_{\vec{X}_i\in\Omega}|\vec{u}_d(\vec{X}_i)|^2}} \tag{16}$$

where $\vec{X}$ is the reference Lagrangian coordinate system, related to Eulerian coordinates through the relation $\vec{x} = \vec{X} + \vec{u}(\vec{X})$, and $\vec{u}$ is produced by any of the eight cases described in Section III-C3. A value of $E_{\mathrm{forw}} \to 0$ reflects a high similarity, while high values reflect differences in the two deformation fields.

2) Evaluation of the Deformation Fields From Reconstruction: Evaluation of the reconstruction models was conducted in terms of the composite deformation field of the forward model and the reconstruction. Denote the reconstruction deformation field by $\vec{u}_r$. A composition of $\vec{u}_d$ and $\vec{u}_r$ yields the composite field $\vec{u}_c$ as

$$\vec{u}_c = \vec{u}_d + \vec{u}_r(\vec{X} + \vec{u}_d). \tag{17}$$

A value of $|\vec{u}_c| \to 0$ indicates a pointwise good reconstruction. The reconstructed deformation field was also investigated in terms of infinitesimal volume changes, or rather as area changes for our 2-D digital phantom where motion in the third direction was not measured. As a measure of the error contained within the restored image, within the deformation field $|\vec{u}_c|$, and within the estimated volume changes, we computed the relative root-mean-square values

$$E_f(f,\vec{u}_c) = \sqrt{\frac{\sum_{\vec{X}_i\in\Omega}\left(f(\vec{X}_i + \vec{u}_c(\vec{X}_i)) - f(\vec{X}_i)\right)^2}{\sum_{\vec{X}_i\in\Omega} f(\vec{X}_i)^2}}$$

$$E_{\mathrm{rel}}(\vec{u}_c,\vec{u}_d) = \sqrt{\frac{\sum_{\vec{X}_i\in\Omega}|\vec{u}_c(\vec{X}_i)|^2}{\sum_{\vec{X}_i\in\Omega}|\vec{u}_d(\vec{X}_i)|^2}}$$

$$E_{\mathrm{vol}}(\vec{u}_c) = \sqrt{\sum_{\vec{X}_i\in\Omega}(\nabla\cdot\vec{u}_c(\vec{X}_i))^2}. \tag{18}$$

A successful reconstruction will lead to $\{E_f, E_{\mathrm{rel}}, E_{\mathrm{vol}}\} \to 0$. All code was implemented in MATLAB, and classification trees were generated by `CLASSREGTREE`.

TABLE II
SUMMARY OF THE MODEL AND IMAGE FEATURES WITH A DESCRIPTION OF THEIR EFFECTS OF THE VARIOUS PARAMETERS

Model Features	Image Features
Heterogeneous	*Undersampling*
Assigns regional parameter values to segmented regions	Controls image noise (SNR)
Poroelasticity	*Gridding*
Controls use of poroelasticity or elasticity in the deformation model	Imposes a grid simulating maximal image contrast and image features
Irregularity	
Adds local variations to the regional parameter maps	

IV. Experimental Results

We performed two different types of numerical experiments with several different parameter settings. First, we compared the deformations from models of different level of complexity (forward problem). Second, we evaluated different image registration approaches to reconstruct the inverse deformations produced by the forward model (inverse problem).

A. Comparing Forward Deformation Fields

We compared the eight deformation fields described in Section III-C3 to $\vec{u}_d$, the deformation field of the default model. Model and image features are shown in Table II, and results are summarized in Table III. The results show that irregularities in the Lamé parameters and permeability have little impact on the forward deformation field, whereas heterogeneous tissue parameters and as well as poroelasticity have a major impact on the deformation field. Additionally, poroelasticity has a damping effect on the deformation (see column relative to $|\vec{u}|$). The average values of the deformation fields produced with "Poroelasticity ON" and "Poroelasticity OFF" were 1.37 and $2.26\,\mathrm{mm}$, respectively, corresponding to a 39.3% reduction in deformation for the poroelasticity model compared to linear elasticity.

We conducted a *k*-means classification of relative differences $E_{\mathrm{forw}}(\vec{u},\vec{u}_d)$ into three classes, "Low," "Medium," and "High." Fig. 5 shows the classification tree of this categorization

TABLE III
RELATIVE DIFFERENCE $E_{\mathrm{forw}}(\vec{u}, \vec{u}_d)$ BETWEEN FORWARD EXPLORED CONFIGURATIONS AND THE DEFAULT FORWARD CONFIGURATION ("HETEROGENEOUS ON," "POROELASTICITY ON," AND "IRREG ON")

Heterogeneous	Poroelasticity	Irreg	$E_{\mathrm{forw}}(\vec{u}, \vec{u}_d)$	$\|\vec{u}\|(mm)$
(default) ON	ON	ON	0.000	1.680
ON	ON	OFF	0.019	1.657
ON	OFF	ON	0.542	2.172
ON	OFF	OFF	0.526	2.136
OFF	ON	ON	0.640	1.073
OFF	ON	OFF	0.645	1.063
OFF	OFF	ON	0.706	2.366
OFF	OFF	OFF	0.705	2.343

Irregular Lamé parameters and permeability have the lowest impact on the deformation field. On the other hand, imposing heterogeneous parameters and poroelasticity have a major impact on the deformation field. The last column shows the average absolute deformation field in millimeter. The first row has a relative difference of zero because these settings correspond to the default configuration, and the deformation field was therefore compared to itself.

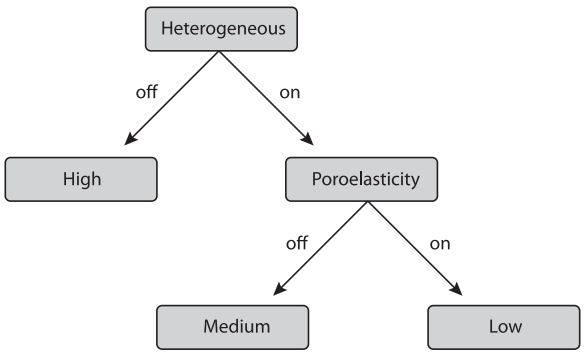

Fig. 5. Classification tree for forward deformations and classes of low, medium, and high relative error.

for various settings of the forward simulations. Heterogeneous/homogeneous tissue parameters is the single most differentiating factor, while linear elasticity/poroelasticity is the second most important factor. Irregular tissue parameters were not significant compared to the other factors and irregularity is, therefore, not included in the classification tree.

B. Comparing FAIR With Biot Registration

To ensure that the performance of the Biot registration was within expected accuracy, we compared its registration with the one produced by the state-of-the-art software FAIR [10]. FAIR has no built-in option for poroelasticity, but it has an option for linear elasticity. Instead of poroelasticity, we, therefore, used linear elasticity for both FAIR and Biot registration. Also, FAIR does not enable heterogeneous tissue parameters. Thus, the tissue parameters in Biot registration were set to "Heterogeneous OFF," with values as in Table I. For the same reason, the configuration with irregular Lamé parameters was not possible to study, and was consequently set to "Irreg OFF."

Valid for both FAIR and Biot registration, the options "Undersampling" and "Gridding" led to the four tests reported in Table IV. The performance of each of the configurations was tested against the default forward deformation field $\vec{u}_d$ using the evaluation metric in (18). The results show that the Biot registration has the smallest error for these evaluation metrics.

C. Evaluating the Quality of the Restored Deformation Field for Various Parameter Configurations

We computed the average reconstruction error for each choice of model ("Heterogeneous," "Poroelasticity," and "Irreg") and image features ("Undersampling" and "Gridding") and switch ("ON" and "OFF") for the Biot registration. The results, measured using (18), are reported in Table V. The overall best performance for the entire image was obtained for "Gridding ON." The application of poroelasticity (option "Poroelasticity") and irregular Lamé parameters/permeability (option "Irreg") have minor impact on the reconstruction performance by image registration.

In order to relate the configuration and performance, a linear regression of the predictors (switches) and the response variable (E_{rel}) was computed and is reported in Table VI. The coding of categorical variables in the regression is "OFF $= 0$" and "ON $=$ 1." The linear regression indicates that the error tends to increase for images with noise (corresponding to 'Undersampling') as the computed coefficient b_4 is positive, while the b_5 coefficient (corresponding to "Gridding") is the negative coefficient with largest absolute value, meaning that tagging has the strongest positive effect insofar the reduction of the error is concerned.

A classification tree with important factors for a restored deformation field with errors "Low," "Medium," or "High" is reported in Fig. 6. Apparently, imposing a gridding pattern on the image has the largest positive impact on registration accuracy as the errors are the lowest for "Gridding ON." The second most discriminating factor is noise/undersampling, leading to lower accuracy for added noise.

V. DISCUSSION

The study is motivated by the demand for improved methods for medical image registration. In particular, we focus on image registration of dynamic time series within the abdomen. Motion corrected time series can advance the field of pharmacokinetic modeling in terms of accuracy and clinical relevance. Moreover, we want to broaden the concept of image registration as a method not only counteracting undesired motion artifacts, but as an investigative tool that can reflect underlying tissue stiffness. In this sense, attributes of the deformation field could serve as biomarkers for pathology. To create a ground-truth deformation, a novel contribution of this study is the implementation of forward simulation of a highly realistic organ system, including heterogeneous and irregular tissue parameters, as well as a poroelastic deformation model. The deformed image from the physically most realistic forward simulation was later used to restore the inverse deformation field. An evaluation of the registration was conducted on the composite deformation field of the forward and restoring deformation fields.

The results obtained by comparing the default forward simulation with the different parameter settings (cfr., Table III and Fig. 5) show that the relative error is dominated by the choice of heterogeneous versus homogeneous tissue parameters. This

TABLE IV
RELATIVE REGISTRATION ERRORS ACCORDING TO (18) FOR COMPARABLE SETTINGS OF FAIR AND BIOT REGISTRATION

Implementation	Undersampling	Gridding	$E_{\mathrm{image}}(f,\vec{u}_c)$	$E_{\mathrm{rel}}(\vec{u}_c,\vec{u}_d)$	$E_{\mathrm{vol}}(\vec{u}_c)$
FAIR	OFF	OFF	0.001	0.915	0.071
	ON	OFF	0.003	0.926	0.071
	OFF	ON	0.044	0.858	0.068
	ON	ON	0.044	0.861	0.068
Mean			0.023	0.890	0.070
Biot registration	OFF	OFF	0.001	0.872	0.069
	ON	OFF	0.005	0.997	0.074
	OFF	ON	0.020	0.320	0.048
	ON	ON	0.021	0.341	0.051
Mean			0.012	0.633	0.061

The Biot registration has a lower average error for all three tested metrics used for evaluation. In particular, there was a larger difference for the "gridding" option.

TABLE V
AVERAGE ERROR PER CONFIGURATION SWITCH USING THE BIOT REGISTRATION FOR DISCRETIZATION

Variable	State	$E_{\mathrm{image}}(f,\vec{u}_c)$	$E_{\mathrm{rel}}(\vec{u}_c,\vec{u}_d)$	$E_{\mathrm{vol}}(\vec{u}_c)$
Heterogeneous	OFF	0.0140	0.6844	0.0625
	ON	0.0130	0.6721	0.0787
Poroelasticity	OFF	0.0146	0.7001	0.0697
	ON	0.0124	0.6525	0.0697
Irreg	OFF	0.0145	0.6997	0.0696
	ON	0.0124	0.6530	0.0698
Undersampling	OFF	0.0119	0.6347	0.0655
	ON	0.0153	0.7232	0.0739
Gridding	OFF	0.0029	0.9562	0.0757
	ON	0.0243	0.4017	0.0637

The largest improvement in E_{rel} occurs for "gridding ON," while the errors in volume estimations E_{vol} are largely independent of the configuration. Generally, the restored deformation field has an relative error E_{rel} in the range of 40–96%. The restored image, as measured by the error $E_{\mathrm{image}}(f,\vec{u}_c)$, is of good quality for all configurations.

TABLE VI
LINEAR REGRESSION APPLIED TO THE MODEL $E_{\mathrm{rel}} = b_0 + b_1 * Heterogeneous + b_2 * Poroelasticity + b_3 * Irreg + b_4 * Undersampling + b_5 * Gridding$, WITH THE VARIOUS PREDICTORS CATEGORIZED AS "OFF= 0" OR "ON = 1"

Predictor	Est. b_i	SE	tStat	pValue
Heterogeneous	-0.0038	0.0434	-0.0870	0.9312
Poroelasticity	-0.0430	0.0434	-0.9904	0.3299
Irreg	-0.0421	0.0434	-0.9705	0.3396
Undersampling	0.0885	0.0427	2.0727	0.0469
Gridding	-0.5545	0.0427	-12.9841	$< 10^{-4}$

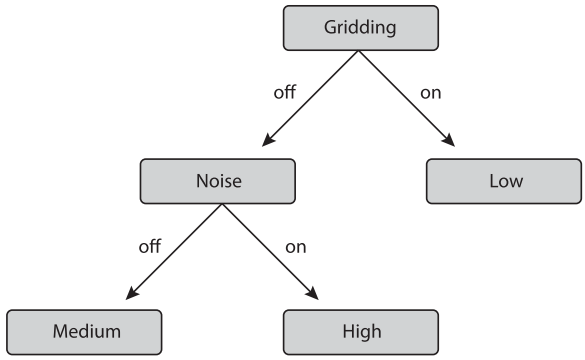

Fig. 6. Classification tree for restoring the deformation field. Adding a tagging to the image has the largest positive impact on the error since a "Low" outcome is obtained with "Gridding ON," The second most important factor is noise/undersampling, where the error becomes "High" with "Undersampling ON."

is probably expected as there are highly varying tissue parameters associated with bone compared to soft tissue. Surprisingly, this type of heterogeneities have not been investigated properly within the field of image registration. Moreover, we found a clear difference in forward simulations created with and without poroelasticity, poroelasticity accounting for a 39.3% reduction in the deformation field magnitude, compared with linear elasticity. These results indicate that the poroelastic damping effect from fluid being dislocated within the void space of the tissue affects the resulting motion significantly. Thus, an important outcome of these simulations is that poroelastic effects as well as heterogeneous tissue parameters are significant factors for this type of deformations and should be applied in simulations of human abdomen.

Biot registration for computing the inverse deformation field was checked for accuracy against the state-of-the-art software for registration FAIR [10] on a reduced set of configurations for compatibility with FAIR. The average restored deformation fields using Biot registration had a lower average error than FAIR (cfr., Table IV). The reasons for this discrepancy is unclear, but it can originate from different interpretations of the scaling force factor γ. However, the incentive of our comparison was not a comprehensive intersoftware comparison of performance, but rather to confirm that our method had a comparable performance to existing methods for registration.

The overall results from restoring the inverse deformation field show that configurations related to image features are dominating the performance. As reported in Fig. 6 and Table VI, adding an artificial gridding as well as noise-free conditions improved the registration performance the most, and heterogeneous parameters, poroelasticity, and irregularities in the tissue parameters were insignificant factors. This result represents a major contribution to the field of image registration, and the result is surprising compared with the forward simulations where heterogeneous parameters as well as poroelasticity had great

impact on the deformation field. The reasons for this discrepancy are unclear, but can probably relate to the type of force being applied. The forward simulation has implemented a volume force decoupled from image features, and the backward simulation of image registration has a force (SSD), which is entirely depending on image features, and is thereby, differently distributed. Most force fields used in image registration are nonzero at locations with a measured discrepancy between the input and target image. Apart from these locations, the force will be small. This property leads to heavily distributed forces along edges. However, in real-world situations, the force is not necessarily devoted to visible edges but rather associated with muscle activity. One possible way to approach this problem could, therefore, be to distribute the registration force according to predefined probabilities of existing muscle activity. However, this would evidently lead to a more complex reconstruction model.

It is surprising that the overall best registration performance in our simulations had a relative error in the absolute deformation field in the range of no better than 40%. In light of these results, one can hardly state that image registration is able to restore the inverse deformation field, but only claim that the relative error in image similarity values is low (0.29–2.4%), in agreement with traditional image registration assumptions. With existing methods, in particular existing force fields, one cannot expect to restore a physically correct deformation field. On the other hand, the restored deformation field can still provide clinically valid information on tissue properties, e.g., by comparing left/right kidneys and in between subjects.

Estimation of tissue stiffness parameters (e.g., μ and λ) as performed in MRE would be a useful task also within the proposed method. However, adding further unknowns to the equations would lead to an underdetermined system, and therefore, require further assumptions for solvability. Future work should investigate whether it would be possible to jointly estimate both the deformation field and tissue stiffness parameters using image registration.

Another interesting observation potentially important for clinical decision making, is that errors related to volume changes (the first tensor invariant, $tr(\epsilon)$) were much smaller ($6.25\% - 7.87\%$) than those seen for the absolute deformation ($40\% - 95\%$). Moreover, the error was essentially independent of discretization and image features. Using the volume changes instead of the absolute deformation as an image derived biomarker is, therefore, highly promising and should be further investigated. Of special relevance is noninvasive assessment of pathological changes in elastic properties of tissue, like in fibrosis and sclerosis, and volume changes can potentially reflect degrees of vascularization and compressibility. The two remaining tensor invariants ($I_2 = (1/2)((tr(\epsilon))^2 - tr(\epsilon^2)), I_3 = det(\epsilon)$) are also interesting in the context of image biomarkers as they are sensitive toward shape change, in particular applied to the deviatoric strain tensor where volumetric changes have been neutralized.

The methodology of linear (poro-) elasticity imposes no limitations on the number of spatial dimensions, nor does the numerical implementation of the MPSA method. However, our digital phantom was restricted to 2-D in order to create a more transparent benchmarking test case. This might be a limitation and future work should include 3-D simulations.

The choice of linear elasticity for our simulations can also be discussed in the context of limitations. Approximations within linear elasticity can be split into geometrical and physical linearities [4]. Geometrical linearity expressed as $|\nabla u| << 1$ and the equality assumption of Eulerian and Lagrangian coordinates lead to the approximation $E \approx e \approx \epsilon$ for the Green strain tensor E, Eulerian strain tensor e, and the infinitesimal strain tensor ϵ. Physical linearity is assumed by developing the strain invariants only up to first order. This leads to the linear stress–strain relation, $\sigma = \sigma(\epsilon)$, known as Hook's law. Within the elastic range of Hook's law, misbehavior of linear elasticity is predominantly associated with large deformations when the Eulerian coordinates no longer are close to the Lagrangian coordinates, or for large rotations [9]. The motion pattern we are investigating occurs from abdominal breathing. This type of motion has negligible rotational components, but may still exhibit medium large deformations in the order of millimeters. However, related to the object investigated, the relative elongation is small in our data, measured to at most $< 3\%$ for the kidney, which is within linear stress–strain range for various soft tissue [36], [37]. Piecewise, linear elastic behavior is typically expected for small and medium large strains [38]. The strain value where an abrupt change in linear modulus takes place varies between tissue types, but it typically occurs at a stress value of several order magnitude higher than the maximum stress in our simulations ($\sigma_{\max} = 0.07\,\mathrm{kPa}$). Based on these arguments we hypothesize that breathing induced abdominal motion predominantly exhibits a linear stress–strain relationship.

However, it is important to keep in mind that human abdomen has a highly complex architecture and consists of a large number of inhomogeneous tissue, exhibiting varying properties with respect to inhomogeneities, anisotropy, as well as creep and stress relaxation. Thus, we consider linear elasticity to be a first approximation to abdominal motion simulations, and future research should explore the impact of more advanced nonlinear, viscoelastic, and hyperelastic deformation models [4]. A potential clinical validity of the proposed methods will have to be confirmed in future studies correlating deformation field attributes to clinical biomarkers from biopsy samples.

VI. Conclusion

Our results show a discrepancy between factors important in the forward simulation and the backward registration. We believe that this discrepancy is due to the different nature of the force applied in the forward and backward scenarios. The registration force is essentially unphysical as it is decoupled from muscle activity, and further efforts should, therefore, be taken to uncover physically more realistic force fields useful for registration. This could potentially also lead to a better registration performance as measured by the absolute deformation field. On the other hand, we found that volume changes are robust, as well as relatively accurate and independent from discretization and image features. Thus, volume changes

could be used for registration generated biomarkers extracted from the deformation field. Such information could generate clinically relevant tissue information reflecting pathology changing elastic properties of tissue, like fibrosis and sclerosis.

ACKNOWLEDGMENT

The authors would like to thanks J. Rørvik at the Department of Radiology, University of Bergen, as well as the kidney project group in MedViz for providing the DCE-MRI image data used to create the geometry of the digital phantom. J. M. Nordbotten is currently associated with the Norwegian Academy of Science and Letters through VISTA, a basic research program funded by Statoil, conducted in close collaboration with the Norwegian Academy of Science and Letters.

REFERENCES

[1] B. Zitová and J. Flusser, "Image registration methods: A survey," *Image Vis. Comput.*, vol. 21, no. 11, pp. 977–1000, 2003.

[2] E. Hodneland *et al.*, "Normalized gradient fields and mutual information for motion correction of DCE-MRI images," in *Proc. 8th Int. Symp. Image Signal Process.*, 2013, pp. 516–521.

[3] T. Rohlfing, "Image similarity and tissue overlaps as surrogates for image registration accuracy: Widely used but unreliable," *IEEE Trans. Med. Imag.*, vol. 31, no. 2, pp. 153–163, Feb. 2012.

[4] W. Maurel *et al.*, *Biomechanical Models for Soft Tissue Simulation*. New York, NY, USA: Springer, 1998.

[5] G. A. Holzapfel, "Biomechanics of soft tissue," in *The Handbook of Materials Behavior Models*, vol. 3. Boston, MA, USA: Academic, 2001, pp. 1049–1063.

[6] C.-Y. Huang *et al.*, "Anisotropy, inhomogeneity, and tension–Compression nonlinearity of human glenohumeral cartilage in finite deformation," *J. Biomech.*, vol. 38, no. 4, pp. 799–809, 2005.

[7] S. Cotin *et al.*, "Real Time Volumetric Deformable Models for Surgery Simulations," in *Visualization in Biomechanical Computing*. New York, NY, USA: Springer, 1996, pp. 535–540.

[8] S. Cotin *et al.*, "Real-time elastic deformations of soft tissues for surgery simulation," *IEEE Trans. Vis. Comput. Graph.*, vol. 5, no. 1, pp. 62–73, Jan.–Mar. 1999.

[9] J. N. Reddy, *An Introduction to Continuum Mechanics*. Cambridge, U.K.: Cambridge Univ. Press, 2008.

[10] J. Modersitzki, *FAIR: Flexible Algorithms for Image Registration*. Philadelphia, PA, USA: SIAM, 2009.

[11] A. Bruhn *et al.*, (2006, Dec.). A multigrid platform for real-time motion computation with discontinuity-preserving variational methods. *Int. J. Comput. Vision* [Online]. *70(3)*, pp. 257–277. Available: http://dx.doi.org/10.1007/s11263-006-6616-7

[12] N. D. Cahill *et al.*, "A demons algorithm for image registration with locally adaptive regularization," in *Medical Image Computing and Computer-Assisted Intervention* (Lecture Notes in Computer Science). G.-Z. Yang, D. J. Hawkes, D. Rueckert, J. A. Noble, and C. J. Taylor, Eds., vol. 5761. New York, NY, USA: Springer, 2009, pp. 574–581.

[13] D. F. Pace *et al.*, (2013, Nov.). A locally adaptive regularization based on anisotropic diffusion for deformable image registration of sliding organs. *IEEE Trans. Med. Imag.* [Online]. *32(11)*, pp. 2114–2126. Available: http://dx.doi.org/10.1109/TMI.2013.2274777

[14] M. Biot, "General theory of three dimensional consolidation," *J. Appl. Phys.*, vol. 12, pp. 155–164, 1941.

[15] P. Drysdale *et al.*, (2010, Aug.). Spatiotemporal bold dynamics from a poroelastic hemodynamic model. *J. Theoretical Biol.* [Online]. *265(4)*, pp. 524–534. Available: http://dx.doi.org/10.1016/j.jtbi.2010.05.026

[16] A. A. Linninger *et al.*, (2009, Apr.). Normal and hydrocephalic brain dynamics: The role of reduced cerebrospinal fluid reabsorption in ventricular enlargement. *Ann. Biomed. Eng.* [Online]. *37(7)*, pp. 1434–1447. Available: http://dx.doi.org/10.1007/s10439-009-9691-4

[17] F. Liu *et al.*, "Model-based estimation of ventricular deformation in the cat brain," in *Proc. Med. Image Comput. Comput.-Assist. Interv.*, 2009, pp. 308–315.

[18] M. M. Mokhtarudin and S. Payne. (2015, May). Mathematical model of the effect of ischemiareperfusion on brain capillary collapse and tissue swelling. *Math. Biosci*. [Online]. *263*, pp. 111–120. Available: http://dx.doi.org/10.1016/j.mbs.2015.02.011

[19] S. R. Mousavi *et al.*, (May 2014). Measurement of in vivo cerebral volumetric strain induced by the valsalva maneuver. *J. Biomech*. [Online]. *47(7)*, pp. 1652–1657. Available: http://dx.doi.org/10.1016/j.jbiomech.2014.02.038

[20] B. R. Simon *et al.*, "Porohyperelastic-transport-swelling theory, material properties and finite element models for large arteries," *Int. J. Solids Structures*, vol. 35, pp. 5021–5031, 1998.

[21] K.-H. S. verud, "Relation between the Chiari Imalformation and syringomyelia from a mechanical perspective," Ph.D. dissertation, Department of Informatics, Faculty of Mathematics and Natural Sciences, University of Oslo, Oslo, Norway, 2014.

[22] J. Kim *et al.*, "Stability, accuracy, and efficiency of sequential methods for coupled flow and geomechanics," *SPE J.*, vol. 16, pp. 249–262, 2011.

[23] K. Vafai, *Handbook of Porous Media, (2nd ed.)* [Online]. New York, NY, USA: Taylor & Francis, 2005. Available: http://books.google.no/books?id=5JNjIM2pRzUC

[24] R. Chandrashekara *et al.*, "Nonrigid image registration with subdivision lattices: Application to cardiac MR image analysis," in *Proc. Med. Image Comput. Comput.-Assist. Interv.*, 2007, pp. 335–342.

[25] M. Ledesma-Carbayo *et al.* (2006). Fully automatic cardiac motion estimation from tagged MRI using non-rigid registration techniques. presented at Computers in Cardiology [Online]. pp. 305–308. Available: http://ieeexplore.ieee.org/stamp/stamp.jsp?arnumber=4511849

[26] M. L. Shehata *et al.* (2009). Myocardial tissue tagging with cardiovascular magnetic resonance. *J. Cardiovascular Magn. Reson.* [Online]. *11(1)*, p. 55. Available: http://dx.doi.org/10.1186/1532-429X-11-55

[27] S. De *et al.*, *Computational Modeling in Biomechanics*. New York, NY, USA: Springer, 2010.

[28] J. M. Nordbotten. (2014, Aug.). Cell-centered finite volume discretizations for deformable porous media," *Int. J. Numer. Meth. Eng.* [Online]. *100(6)*, pp. 399–418. Available: http://dx.doi.org/10.1002/nme.4734

[29] J. M. Nordbotten. (May 2014). Finite volume hydromechanical simulation in porous media. *Water Resources Res.* [Online]. *50(5)*, pp. 4379–4394. Available: http://dx.doi.org/10.1002/2013WR015179

[30] I. Aavatsmark, "An introduction to multipoint flux approximations for quadrilateral grids," *Comput. Geosci.*, vol. 6, pp. 405–432, 2002.

[31] R. M. Berne , *et al.*, *Physiology, 5th ed*. New York, NY, USA: Elsevier, 2004.

[32] W. F. Boron and E. L. Boulpaep, *Medical Physiology*. New York, NY, USA: Elsevier Health Sciences, 2008.

[33] J. Berliner and R. W. Orloff, *Renal Physiology*. Bethesda, MD, USA: Amer. Physiol. Soc., 1973.

[34] H.-C. Spatz *et al.*(1996, Mar.). Youngs moduli and shear moduli in cortical bone. *Proc. Roy. Soc. B, Biol. Sci.* [Online]. *263(1368)*, pp. 287–294. Available: http://dx.doi.org/10.1098/rspb.1996.0044

[35] X. Chen *et al.* (2011). Identification of physical properties of swine liver for surgical simulation using a dynamic deformation model. in *Proc. IEEE/SICE Int. Symp. Syst. Integration (SII) [Online]*.pp. 655–660. Available: http://ieeexplore.ieee.org/stamp/stamp.jsp?arnumber=6147526

[36] W. Decraemer *et al.*, "An elastic stress-strain relation for soft biological tissues based on a structural model," *J. Biomech.*, vol. 13, no. 6, pp. 463–468, 1980.

[37] Y.-C. Fung, "On mathematical models of stress-strain relationship for living soft tissues," *Polymer Mech.*, vol. 11, no. 5, pp. 726–740, 1975.

[38] F. A. Duck, *Physical Properties of Tissues: A Comprehensive Reference Book*. New York, NY, USA: Academic, 2013.

Authors' photographs and biographies not available at the time of publication.